ACS OMEGA

http://pubs.acs.org/journal/acsodf

Article

Novel Biogenic Synthesis of a Ag@Biochar Nanocomposite as an Antimicrobial Agent and Photocatalyst for Methylene Blue Degradation

Abdelazeem S. Eltaweil,* Ahmed M. Abdelfatah, Mohamed Hosny,* and Manal Fawzy

Cite This: *ACS Omega* 2022, 7, 8046−8059

Read Online

ACCESS | Metrics & More | Article Recommendations | Supporting Information

ABSTRACT: The conventional synthesis of nanomaterials employing physical and chemical methods usually requires high cost and toxic chemicals. Thus, a facile, ecofriendly, cost-effective, novel, and sustainable route for the synthesis of a silver-loaded biochar nanocomposite (Ag@biochar) using *Chenopodium ambrosioides* leaf extract and biomass is reported for the first time in this study to advocate many of the principles of green chemistry such as safer solvents and auxiliaries. UV spectroscopic analysis at 420 nm indicated the formation of silver nanoparticles (AgNPs). The band gap energy of Ag@biochar was 1.9 eV, confirming its potential use as a photocatalyst. Ag@biochar was found to be photoluminescent at 425 nm. AgNPs on the surface of biochar were predominantly spherical with a size range of 25−35 nm and a surface area of 47.61 m^2/g. A zeta potential of −5.87 mV designated the stability of Ag@biochar. Testing the photocatalytic potential of Ag@biochar to remove methylene blue from wastewater demonstrated its high removal efficiency that reached 88.4% due to its high efficiency of electron transfer confirmed *via* electrochemical impedance spectroscopy analysis and retained 70.65% after six cycles of reuse. Ag@biochar was shown to be a powerful broad-spectrum antimicrobial agent as it completely prevented the growth of *Escherichia coli* and also inhibited the growth of *Pseudomonas aeruginosa*, *Klebsiella pneumoniae*, *Bacillus subtilis*, and *Candida albicans* with the inhibition zones of 19, 18, 22, and 16 mm, respectively.

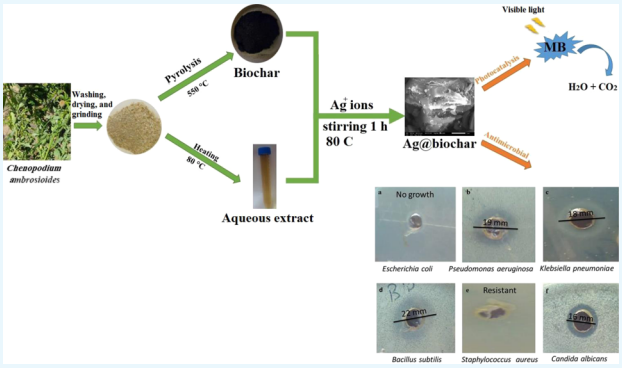

1. INTRODUCTION

There is no doubt that water is an essential resource for sustaining all forms of life, and its treatment, particularly in the industrial sectors, is a necessity to eliminate environmental and health risks.[1−3] Due to technological development and the dramatic increase in industrial activities, the environment has seriously deteriorated, especially the aquatic environment.[4−6] Toxic organic pollutants are important environmental hazards that seriously threaten both aquatic and terrestrial ecosystems.[7−9] Among these organic pollutants, dyes from the textiles and other industries are hazardous effluents containing toxic complex components that without appropriate treatment will severely impact the environment and cause harmful health effects including difficulties in breathing, vomiting, eye burns, allergies and contact dermatitis, and different types of cancer.[10,11] Therefore, how to effectively remediate organic pollution of the environment has become more and more challenging.[12,13]

In recent years, biochar has gradually entered people's vision.[14] Biochar is a carbon-rich solid, which is obtained by heating biomass in an oxygen-depleted environment, such as wood and manure with little or no oxygen.[15] As a kind of adsorbent, biochar, with a porous structure similar to that of activated carbon, is the most commonly used and effective adsorbent in the world to remove various pollutants in water.[16] However, among the limitations of using biochar for wastewater treatment are the relatively low surface area and the influence of abiotic and/or biotic processes which can diminish its effectiveness in certain applications.[17]

Despite several scientific pieces of research on biochar applications, recent researchers have been focused primarily on the modification of the biochar using nanomaterials and other structures to improve its performance in environmental applications and remediation potentials.[18] Numerous methods, such as chemical, physical, mineral impregnation, and magnetic modifications, have been utilized in producing biochar nanocomposites[19,20] for the sake of enhancement of its adsorption, catalytic, and photocatalytic degradation.[21,22] In this regard, various inexpensive metal oxides have been used to

Received: December 21, 2021
Accepted: February 10, 2022
Published: February 21, 2022

https://doi.org/10.1021/acsomega.1c07209
ACS Omega 2022, 7, 8046−8059

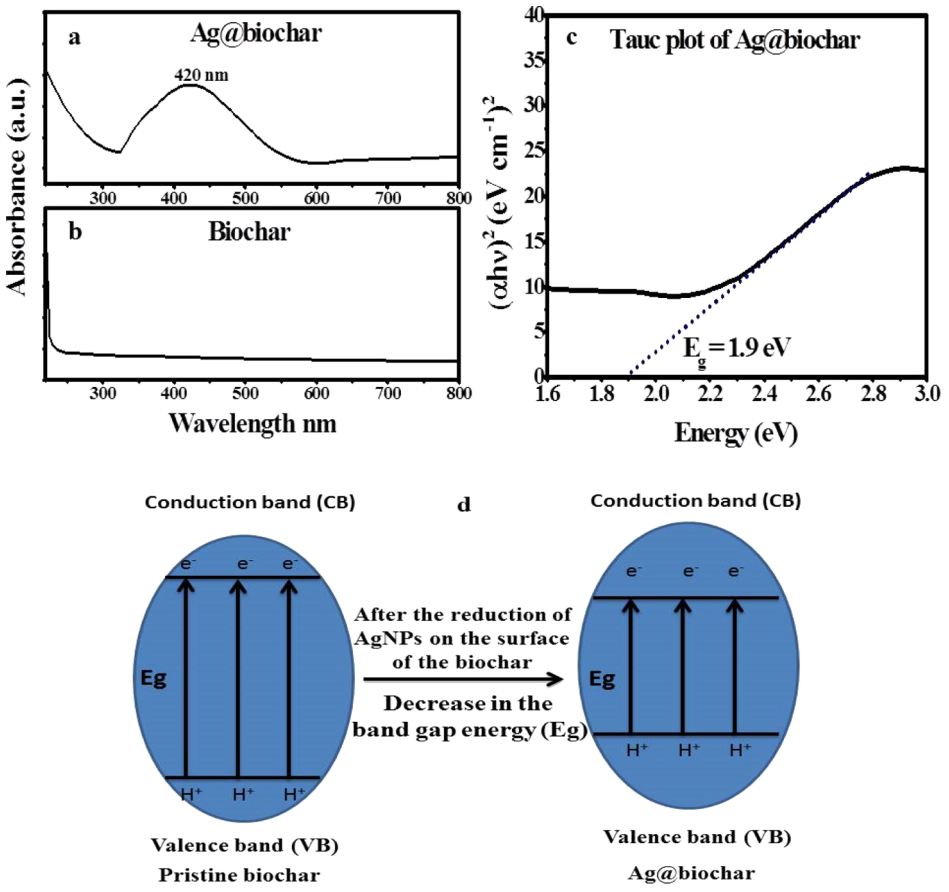

Figure 1. (a,b) UV−visible spectra of Ag@biochar and biochar, (c) Tauc plot of Ag@biochar, and (d) graphical representation of the band gap change between pristine biochar and Ag@biochar.

synthesize composite photocatalysts including $PrVO_4$,[23] $NdVO_4$,[24] Ho_2O_3,[25] and other magnetic nanocomposites such as $Fe_2O_3/EuVO_4/g\text{-}C_3N_4$[26] to remove several organic pollutants including perilous cationic and anionic dyes. Moreover, the production of highly efficient biochar nanocomposites using metallic nanoparticles has been previously proven.[27,28]

Among metal nanoparticles, silver nanoparticles (AgNPs) are predominantly utilized in a variety of medicinal and environmental applications such as diagnosis, cancer treatment, genes, drug delivery and degradation of toxic organic pollutants because of their oxidation resistance, biocompatibility, stability, and optical properties.[29]

In comparison with the conventional chemical and physical synthesis techniques, green synthesis has emerged as an appropriate alternative as it seeks to avoid secondary impacts by either (i) using sustainable materials or (ii) consuming less energy in the synthesis process, aspiring for ambient synthesis reaction conditions. Plant extracts contain phytoconstituents such as flavonoids, terpenoids, and phenolic compounds that have been proven to be efficient reducing and stabilizing agents for the synthesis of metal and metal oxide nanoparticles in a facile and single-step process. In addition, utilizing plant extracts was previously concluded to be resulting in the formation of multiple-shaped nanoparticles as a result of containing various phytoconstituents.[30,31] Therefore, biosynthetic approaches, specifically those using plant extracts, arose as a faster, cheaper, environmentally safer, and more efficient route to synthesize nanomaterials, particularly when compared to previous research works that targeted the synthesis of nanostructures using high temperature and pressure in a hydrothermal procedure,[32−36] as well as other works that aimed for the chemical synthesis of nanomaterials.[37]

As a result of the growing problem of multidrug-resistant bacteria, on which conventional antibiotics have little or no effect, AgNPs have emerged as a proper and alternative antibiotic agent that have been proven to be highly efficient, particularly AgNPs that are synthesized by green synthesis. The antibacterial action of AgNPs has improved on a nanoscale with the emergence of nanotechnology, and currently, it is utilized to manage a variety of human and animal diseases. The material size, capping agent of AgNPs, content, and phytochemical structure are considered to be critical factors in determining their antimicrobial efficacy.

Herein, we aimed to fabricate a Ag@biochar nanocomposite *via* a novel and completely green route for the first time, in which the biomass, *Chenopodium ambrosioides* (*C. ambrosioides*), acts as a green source of biochar and its extract acts as a reducing agent for silver ions, avoiding the use of chemicals in the whole process, which constitutes the novelty of this work. Therefore, the role of *C. ambrosioides* is twofold: first, the production of biochar from readily available biomass and, second, reducing silver ions into AgNPs and supporting them on the biochar. The photocatalytic potential of the phytosynthesized Ag@biochar nanocomposite was evaluated in the removal of methylene blue (MB) from polluted water. Furthermore, the antibacterial and antifungal capabilities of the Ag@biochar nanocomposite were investigated.

https://doi.org/10.1021/acsomega.1c07209
ACS Omega 2022, 7, 8046−8059

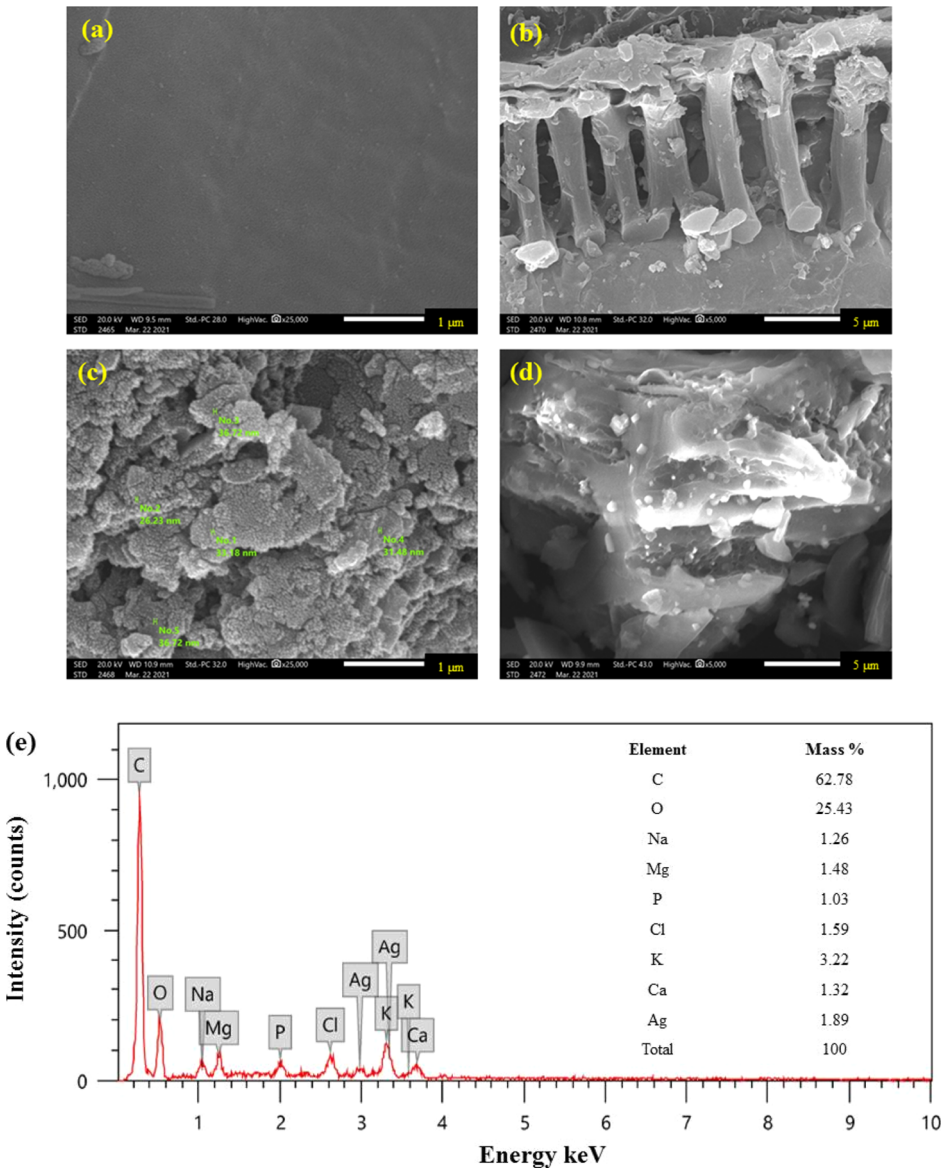

Figure 2. SEM photomicrographs of (a,b) biochar and (c,d) Ag@biochar and (e) EDX analysis.

2. RESULTS AND DISCUSSION

2.1. Characterization of Ag@Biochar. *2.1.1. UV−Visible Spectroscopy.* Generally, UV−visible spectroscopy is deemed to be a very basic and efficient tool that is utilized to indicate the successful reduction of metal salts into nanoparticles such as gold, silver, and platinum. The surface plasmon resonance (SPR) peak of Ag@biochar was quite obvious (Figure 1a) at a wavelength of 420 nm, which is in line with lots of other previous studies that targeted the green synthesis of AgNPs by utilizing extracts of numerous plant species.[38] Regarding the UV−vis spectrum of the pristine biochar, there were no peaks observed at all (Figure 1b). Furthermore, it has been noticed that the band gap energy (E_g) of Ag@biochar was elucidated by the Tauc plot, as shown in Figure 1c. The Kubelka−Munk function $(\alpha h\nu)^2$ was plotted against the band gap energy ($E_g = h\nu = hc\lambda$), where α is the absorption coefficient, h is the Plank constant, and ν is the frequency of radiation. The band gap is then estimated by extrapolating the linear portion of the graph to the y-axis zero value, and it was about 1.9 eV (Figure 1c), which is better than the band gaps of other biochar composites such as TiO_2@biochar[39] and N−biochar composites.[40] Thus, the deposition of AgNPs on the surface of biochar decreases the band gap energy of the pristine biochar, as demonstrated in Figure 1d. This also supports the creation of new energy states in the Ag@biochar nanocomposite samples caused by Ag−C bonds formed as a result of AgNP association with biochar's carbon content. Therefore, Ag@biochar could be harnessed in the photocatalytic degradation of MB.

2.1.2. X-ray Diffraction Analysis. X-ray diffraction (XRD) analysis is an indispensable step in gaining information about the nanomaterials' crystal structure and crystal lattice.[41,42] The XRD spectrum of the pristine biochar (Figure S1a) exhibited characteristic peaks at 28.5, 40.6, and 50.26°, which were indexed to the (002), (100), and (004) planes, respectively, as previously mentioned by other workers,[43] whereas the XRD pattern of the Ag@biochar composite (Figure S1b) demonstrated the same peaks of the pristine biochar yet with a lower intensity and other new peaks at 32.1, 46.06, and 62.5° which were indexed to the (111), (200), and (220) planes, respectively, referring to face-centered-cubic silver (JCPDS

https://doi.org/10.1021/acsomega.1c07209
ACS Omega 2022, 7, 8046−8059

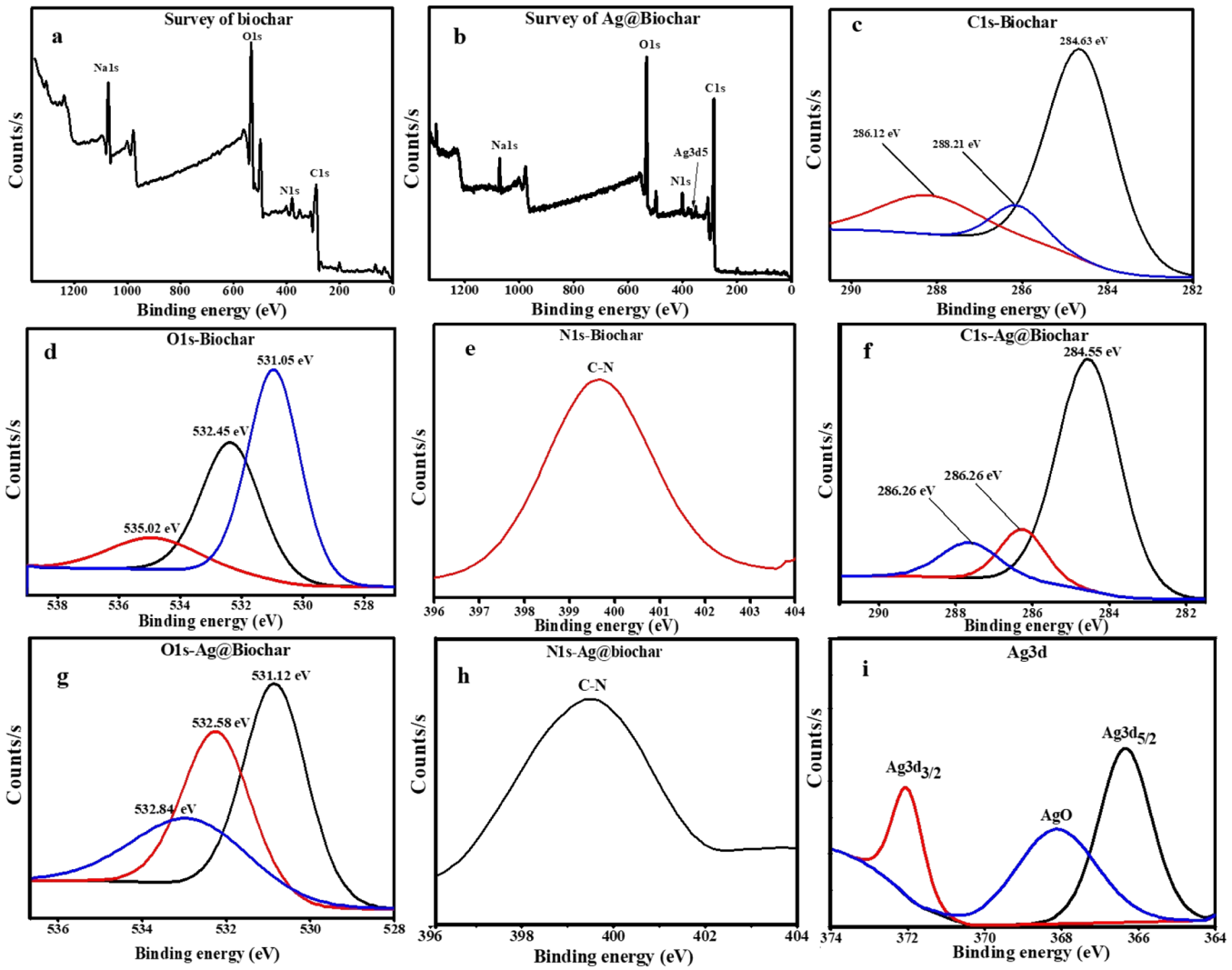

Figure 3. XPS spectra for the biochar survey (a), Ag−biochar survey (b), biochar C 1s (c), O 1s (d), N 1s (e), Ag−biochar C 1s (f), O 1s (g), N 1s (h), and Ag 3d (i).

file number 04-0783). Moreover, the (111) plane, in accordance with many workers,[44] was the preferred growth direction for the phytosynthesized Ag@biochar nanocomposite. When the Scherrer formula[45] was applied to estimate the crystallite size based on the main plane of (111), it was found to be approximately 27 nm, which was close to the size range (25−35 nm) measured by SEM. These findings confirmed the successful reduction of silver ions on the surface of the biochar-producing Ag@biochar nanocomposite.

2.1.3. Fourier Transform Infrared Spectroscopy Analysis. Fourier transform infrared (FT-IR) spectroscopy analysis shown in Figure S1c was carried out to investigate the surface modification of biochar with AgNPs. Some oxygen-containing groups were detected on the surface of the pristine biochar such as the hydroxyl group (OH). A spectral band for the O−H stretching vibration was found at 3274 cm^{-1} that shifted to a lower wavenumber (a lower intensity) at 3308 cm^{-1} in the IR spectrum of Ag@biochar, indicating the role of *C. ambrosioides* phytoconstituents containing OH functional groups such as flavonoids, tannins, and alkaloids[46] upon being oxidized and resulting in the reduction of silver ions into AgNPs on the surface of the biochar. The peaks near 1600 cm^{-1} in both samples were assigned to the aromatic C═O ring stretching, which is also attributed to the same phytoconstituents.[47] Also, the peaks near 1430 cm^{-1} were likely due to the aromatic C−O ring stretching. In addition, other aromatic stretching peaks between 1000 and 1200 cm^{-1} are suggested to be resulting from the incompletely pyrolyzed *C. ambrosioides* feedstock such as cellulose and hemicellulose, as mentioned in previous biochar research articles.[47]

2.1.4. SEM and EDX Analysis. The SEM technique was used to identify the morphological surface features of pristine biochar and biochar after modification with AgNPs and to provide information on the porosity and surface structure of both materials and size and shape of AgNPs that are dispersed on the biochar surface as it was previously utilized by many workers.[48] The pristine biochar and Ag@biochar composite are illustrated in Figure 2a,b and 2c,d in a respective manner. In this study, the SEM images revealed a porous structure in both biochar samples. Porosity is commonly considered as a consequence of the release of matter in the form of small volatile molecules including CO, CO_2, CH_4, and H_2O during the thermal conversion process. The ubiquitous distribution of AgNPs on the surface of biochar is quite obvious in Figure 2c,d as AgNPs appeared as white particles dispersed on the biochar's surface, which was not found in the pristine biochar

https://doi.org/10.1021/acsomega.1c07209
ACS Omega 2022, 7, 8046−8059

sample (Figure 2a,b), thus confirming the successful green synthesis of the Ag@biochar nanocomposite. The appearance of strong signals for elemental Ag at 3 and 3.3 keV in the current study as shown in Figure 2e was similar to previous results that were reported by other workers,[49] confirming the green synthesis of the Ag@biochar nanocomposite. The elemental analysis of the Ag@biochar's surface (Figure 2e) indicated that the total zero-valent Ag percentage in the sample was 1.89%, which is quite close to the percentage of silver ions that were initially dispersed on the surface of the biochar, which was 2% silver, ensuring the great efficacy of the aqueous extract of *C. ambrosioides* in the reduction of silver ions into AgNPs on the biochar's surface. Furthermore, it is to be mentioned that the particle size of the dispersed AgNPs on the surface of the biochar in the current investigation was in the range of 25−35 nm.

2.1.5. XPS Analysis. A further investigation was carried out using X-ray photoelectron spectroscopy (XPS), a powerful surface-sensitive analytical tool, to analyze the chemical compositions, ionic characteristics, and bonding configuration differences between biochar and Ag@biochar. Two major surveys for biochar and Ag@biochar indicate the presence of C 1s, O 1s, N 1s, and Na 1s as major constituents in addition to Ag 3d in the case of the Ag@biochar nanocomposite, as presented in Figure 3a,b, respectively. Figure 3c shows the C 1s spectrum of the biochar, and the different peaks at 284.63, 286.12, and 288.21 eV are attributed to C−C, C═C, C−O, and O−C−O, respectively, which is mainly derived from the polyphenol groups in the plant. In comparison with the C 1s of the Ag@biochar (Figure 3f), there is a noticeable shift in the C−O peak from 288.21 to 286.26 eV, indicating the reduction of Ag ions into silver nanoparticles on the surface of the biochar. The binding energies of the O 1s spectrum of the biochar (Figure 3d) show that the binding energy peaks at 531.05, 532.45, and 535.02 eV were attributed to the O atoms from the sulfonate functional,[50] S═O,[51] and C−O groups,[52] respectively. The O 1s of the Ag@biochar (Figure 3g) shows that there was also an obvious shift in C−O from 535.02 to 532.84 eV, denoting the bonding of AgNPs to the surface of biochar. In addition, the N 1s spectrum of biochar demonstrated the appearance of C−N at 399.66 eV as shown in Figure 3e that shifted to 399.88 eV in the case of Ag@biochar (Figure 3h), indicating the formation of AgNPs and their probable interaction with nitrogen.[53] The deconvoluted peaks of the Ag 3d spectrum (Figure 3i) show the peak binding energies at 366.4, 368.1, and 372.5 eV. Among these, the peak at 368.1 eV corresponded to silver oxide (Ag−O), and the peaks at 366.4 and 372.5 eV corresponded to the unbound Ag $3d_{5/2}$ and Ag $3d_{3/2}$, respectively, of metallic silver nanoparticles as the binding energy splitting value was almost 6 eV, similar to that reported by Ghodake *et al.*[54] The current XPS analysis confirmed the presence of AgNPs and Ag−O, indicating the successful distribution of silver on the surface of the biochar and also the successful reduction of Ag ions into AgNPs on the surface of the biochar.

2.1.6. Zeta Potential. Zeta potential is one of the main tools that are harnessed to express the stability of nanoparticles in an aqueous solution.[55] The recorded zeta potential for the biochar was −9.25 mV, as displayed in Figure S2b, while in the case of the Ag@biochar composite, it was recorded as −5.87 mV, as shown in Figure S2a that was similar to other results.[56] A probable justification for the decrease in the zeta potential value of Ag@biochar compared to the pristine biochar could be the interaction between the biochar and the deposited silver that resulted in the oxidation of some of the functional groups contributing to the negative surface charge such as COOH and OH. Consequently, it was concluded that the Ag@biochar of the current work acquired stable dispersal potential in the solution that remained for almost 1 month and also indicated its potential use as an adsorbent and a photocatalytic material for the removal of cationic dyes such as MB.

2.1.7. Thermal Gravimetric Analysis. The thermogravimetric analysis (TGA) result of biochar and Ag@biochar is shown in Figure 4. The two samples exhibited a first regular

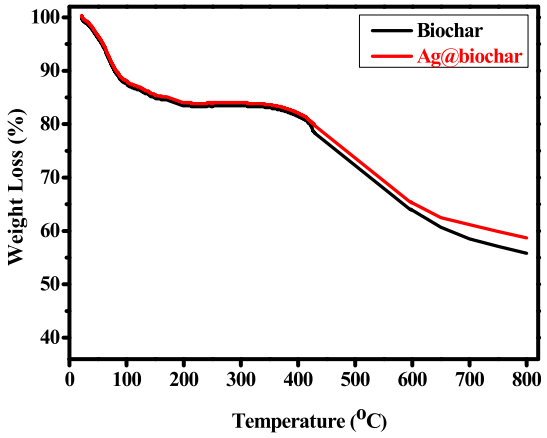

Figure 4. TGA curves of biochar and Ag@biochar.

step with an approximate weight loss of 15% up to 150 °C, which could be attributed to the loss of the moisture content.[57,58] Then, the two samples were almost stable up to 360 °C. After that, there was a rapid weight loss from 360 to 800 °C for both samples, which could be assigned to the decomposition of cellulosic and hemicellulosic compounds, as well as lignin. However, the weight loss of Ag@biochar was less than that of the pristine biochar, which could be accredited to the capability of silver nanoparticles in resisting thermal degradation.

2.1.8. BET Analysis. The surface areas of biochar and Ag@biochar samples were determined using the multipoint Brunauer−Emmett−Teller (BET) method based on the nitrogen adsorption/desorption isotherm, while their total pore volumes were determined using the Barrett, Joyner, and Halenda (BJH) method. Figure 5 represents the N_2 adsorption/desorption isotherms of the biochar and Ag@biochar nanocomposite. It is obvious from the isotherms that both biochar and Ag@biochar exhibit type IV isotherms. The specific surface areas S_{BET} of biochar and Ag@biochar were found to be 64.36 and 47.61 m^2/g, respectively. It is obvious that the specific surface area of pristine biochar decreased upon the incorporation of AgNPs on its surface. In addition, the pore volume of biochar and Ag@biochar were 0.033 and 0.024 m^3/g, respectively.

2.1.9. Photoluminescence Spectroscopy of Ag@Biochar. Noble metal photoluminescence (PL) can be explained as the excitation of electrons from occupied d bands into states above the Fermi level.[59] AgNPs are reported to emit light between 400 and 700 nm, which is caused by the relaxation of the surface plasmon's electronic mobility.[60] When the excitation wavelength was 340 nm, the phytosynthesized Ag@biochar nanoparticles were confirmed to be photoluminescent as the

https://doi.org/10.1021/acsomega.1c07209
ACS Omega 2022, 7, 8046−8059

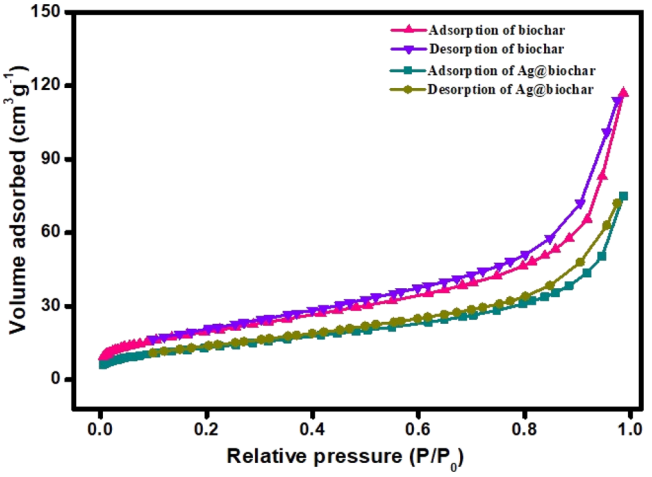

Figure 5. N_2 adsorption/desorption isotherm of biochar and Ag@biochar.

emission wavelength was observed at 425 nm, as shown in Figure 6, which is similar to the PL spectrum reported in another study that targeted the green synthesis of AgNPs.[61]

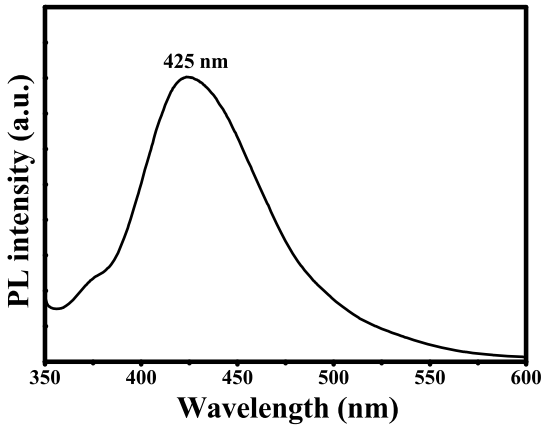

Figure 6. PL spectra of Ag@biochar.

2.1.10. Electrochemical Impedance Spectroscopy of Ag@Biochar. The Nyquist plot can be used to determine the nanomaterial's resistance through the electrochemical impedance spectroscopy (EIS) analysis. This analysis was used to examine the electrochemical performance of the Ag@biochar photocatalyst, and the obtained results are presented in Figure 7. The arc radius resembles the electron transfer efficacy, and it is well established that the smaller the radius, the better the rate of electron transfer.[62] As the arc radius of Ag@biochar was found to be smaller than that of pristine biochar, it was confirmed that Ag@biochar has a faster electron transfer that resulted in its high photocatalytic performance.

2.2. Photocatalytic Study. The photocatalytic efficiency of the green synthesized Ag@biochar nanocomposite toward the photodegradation of MB was investigated by employing a 300 W xenon lamp as a visible-light source (λ > 420 nm), using different concentrations of MB (10−50 ppm). First, 5 mg of the Ag@biochar nanocomposite was dispersed in an aqueous solution and vigorously stirred for 30 min to attain the adsorption/desorption equilibrium and to facilitate the diffusion of MB molecules to the matrix of the nanocomposite before being exposed to visible light to initiate the photo-

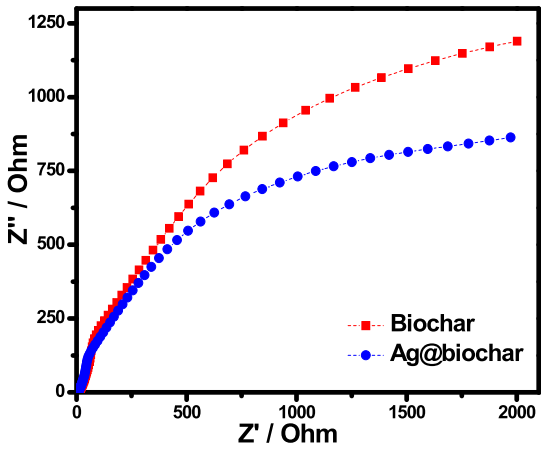

Figure 7. EIS Nyquist plots of biochar and Ag@biochar.

catalytic process. Afterward, the concentration of MB was measured during the reaction course by following the intensity of the characteristic UV−vis absorption peak of MB at 664 nm. As a result, the Ag@biochar nanocomposite exhibited an immediate photocatalytic efficacy of 98.72% at a concentration of 10 ppm (Figure 8a) and the photocatalytic efficiencies of 88.4 and 84% at the concentrations of 25 and 50 ppm in 75 and 210 min, respectively (Figure 8b,c), which was mainly attributed to the synergy between the AgNPs that enhance the visible-light-harvesting capability of the nanocomposite due to the SPR phenomenon and the graphitic structure of the biochar[63] that ameliorates the interfacial charge separation, thus quenching the recombination electron−hole pairs, which in turn improves the generation of reactive oxygen species (ROS) that drive the photocatalytic degradation process. Consequently, it displayed high photocatalytic performance. Remarkably, the UV−vis absorption peak at 664 nm showed a slight blue shift during the reaction course that could be attributed to the diminished ethyl group and benzene ring within the MB structure. However, the Ag@biochar nanocomposite revealed a slight decrease in the photocatalytic efficiency at elevated concentrations of 25 and 50 ppm comparable to 10 ppm that may be caused by the intense color of MB that causes turbidity and thus shields the visible light from striking the photocatalyst.

When the effect of the pristine biochar on the photodegradation of MB was evaluated, it was found that the degradation efficiency was only about 16.35% against MB with a concentration of 25 ppm, as shown in Figure 8d. Additionally, the photocatalytic degradation of MB was tested using only UV irradiation as MB is considered to be a reactive dye that was found to be only 7.38% (Figure 8e). Therefore, it was concluded that Ag@biochar was mainly responsible for the photodegradation of MB.

The kinetics of the photodegradation of MB with the concentration of 25 ppm is presented in Figure 8f, and the rate constant K was found to be 0.0147 min^{-1}, which is higher than that of chemically synthesized AgNPs (0.011 min^{-1}) previously prepared by Ji *et al.*[64] Consequently, it was concluded that Ag@biochar worked as an effective carrier for the photogenerated electrons and was responsible for the production of hydroxyl free radicals that resulted in the photodegradation of MB. Regarding the recycling of Ag@biochar, it was observed that the efficiency diminished from 88.4 to 70.65% after six cycles of reuse (Figure 8g) against MB

https://doi.org/10.1021/acsomega.1c07209
ACS Omega 2022, 7, 8046−8059

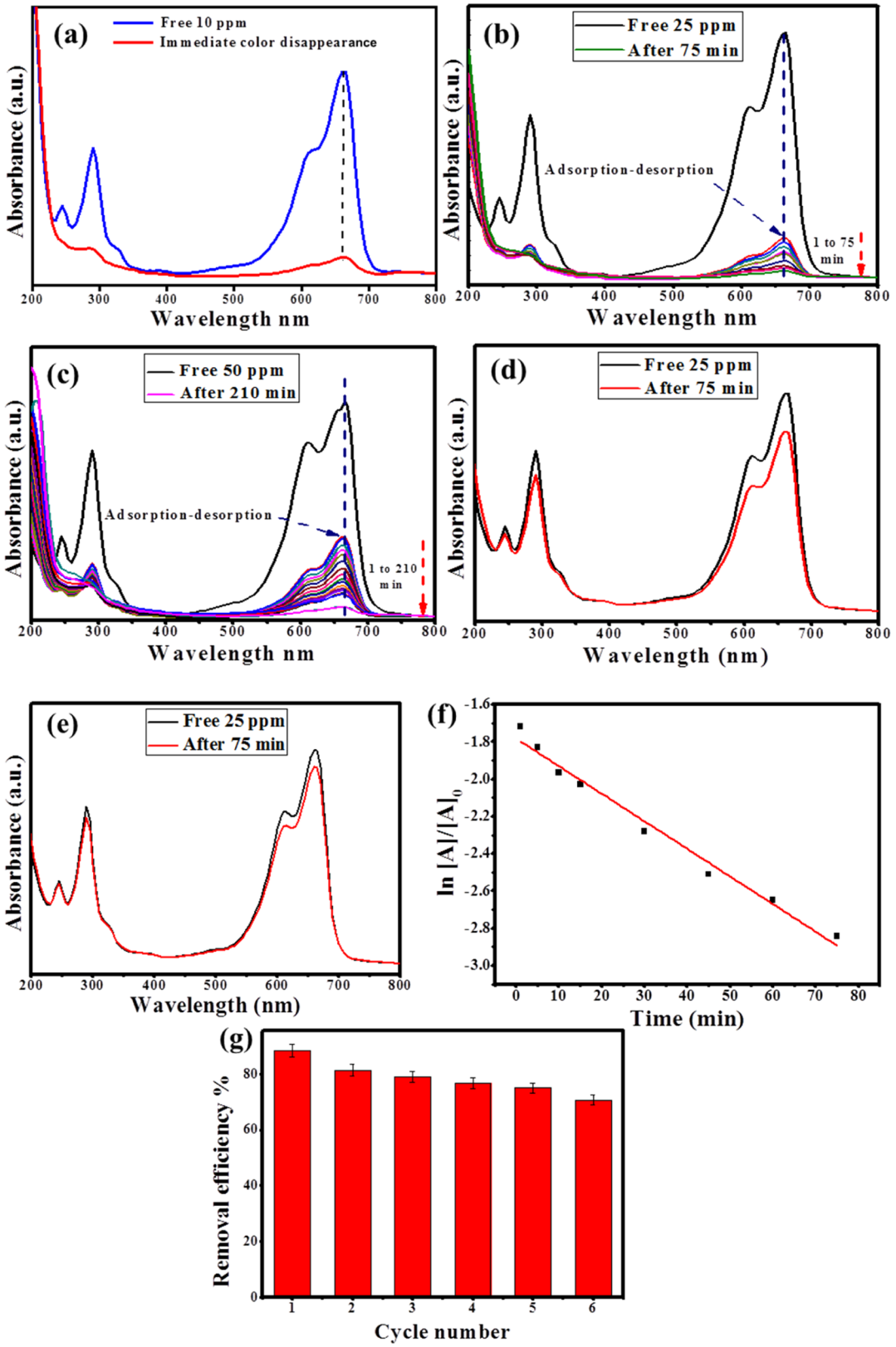

Figure 8. UV−vis absorption spectra of MB degradation with Ag@biochar at different reaction times and different MB concentrations of 10 (a), 25 (b), and 50 ppm (c); photodegradation of MB (25 ppm) using pristine biochar, (d) photodegradation of MB (25 ppm) using only UV irradiation, (e) kinetics of photocatalytic degradation of MB (25 ppm) using Ag@biochar, and (f) recycling of Ag@biochar against MB (25 ppm) (g).

with a concentration of 25 ppm, indicating the good efficiency of Ag@biochar regeneration. The time effect on the photodegradation process of MB at the concentrations of 25 and 50 ppm in the presence of Ag@biochar is shown in Figure S3a,b.

https://doi.org/10.1021/acsomega.1c07209
ACS Omega 2022, 7, 8046−8059

2.2.1. Possible Adsorption and Photocatalytic Mechanism for the Removal of MB by the Ag@Biochar Nanocomposite. First, the high S_{BET} of the Ag@biochar nanocomposite, as well as the presence of a variety of functional groups, increase the opportunity of MB adsorption on the surface of the Ag@biochar nanocomposite. Second, it was well established that cationic dyes could be easily adsorbed on the surface of negatively charged materials *via* electrostatic attraction. Additionally, the presence of other forces such as $\pi-\pi$, n$-\pi$, and H-bonding between MB and the OH groups at the outer surface of biochar enhanced the adsorption capability of MB on the Ag@biochar nanocomposite.[57] Besides, MB could be adsorbed *via* the complexation of AgNPs with the active functional groups of MB.

Moreover, the XPS results confirmed that the binding energy splitting of the synthesized silver is 6 eV, which reflects its presence as Ag^0 in the hybrid photocatalyst and hence the ability to extend the absorption in the visible-light region and its potential to photodegrade toxic organic pollutants,[65] subsequently indicating the efficient photocatalytic degradation efficiency of Ag@biochar, which also could be accredited to the faster electron transfer rate confirmed *via* the EIS analysis. After the initial adsorption process of MB using the Ag@biochar nanocomposite, the removal efficiency of MB with higher concentrations could be attributed to the subsequent photocatalytic process for MB photodegradation. As a result of visible-light irradiation of the Ag@biochar nanocomposite, electron−hole pairs were formed due to the SPR phenomenon of AgNPs generating ROS such as superoxide anions ($^{\bullet}O_2^-$) and hydroxyl radicals ($^{\bullet}OH$) *via* the reaction of free electrons (e^-) with oxygen and the reaction of h^+ with H_2O molecules adsorbed onto the Ag@biochar nanocomposite, respectively, which in turn initiate the photocatalytic degradation of the adsorbed MB molecules. Moreover, the reaction of visible light with oxygen (O_2) could result in the formation of other ROS such as the singlet oxygen ($^1O_2$)[66] that further improves the photodegradation of MB.[67,68] A schematic representation of the possible mechanism for the photocatalytic degradation of MB on Ag@biochar is shown in Figure S4

$$Ag + h\nu\ (\text{visible}) \rightarrow Ag\ (h^+ + e^-) \quad (1)$$

$$e^- + O_2 \rightarrow {}^{\bullet}O_2^- \quad (2)$$

$$h^+ + H_2O \rightarrow H^+ + {}^{\bullet}OH \quad (3)$$

$$O_2 + h\nu\ (\text{visible}) \rightarrow {}^1O_2 \quad (4)$$

$$^{\bullet}O_2^- + {}^{\bullet}OH + {}^1O_2 + MB \rightarrow CO_2 + H_2O + \text{byproducts} \quad (5)$$

To evaluate the photodegradation capacity of the synthesized Ag@biochar, it was compared with other catalysts reported in other research works. Such a comparison is summarized in Table 1 and confirms that Ag@biochar exhibits a good degradation capacity compared to other catalysts and it can be considered as a promising material for the removal of toxic organic pollutants such as MB.

2.3. Antimicrobial Study. *2.3.1. Antibacterial Study.* Metallic nanoparticles are deemed to be useful disinfectant agents such as silver, zinc oxide, and gold nanoparticles, which are the most widely used agents. AgNPs' well-known inhibitory actions have been employed in a variety of medicinal applications, particularly the inhibition of positive and negative bacterial strains. Nanocomposites prepared by mixing AgNPs with other nanoparticles, biopolymers, and other materials have also been proven to have efficient antimicrobial effects.[73,74] Consequently, the antimicrobial efficacy of Ag@biochar synthesized in this study was tested against different Gram-negative and Gram-positive bacteria such as *Escherichia coli*, *Pseudomonas aeruginosa*, and *Klebsiella pneumoniae* (Gram-negative bacteria) and also Gram-positive bacteria including *Bacillus subtilis* and *Staphylococcus aureus*. The obtained results showed that the inhibition zone was 19 mm in the case of *P. aeruginosa*, 18 mm for *K. pneumoniae*, and 22 mm for *B. subtilis*, and no growth was observed at all in the case of *E. coli*, meaning that Ag@biochar was so efficient against *E. coli* as it prevented the growth of the bacteria. The current findings imply that Ag@biochar may have antibacterial properties by altering the structure of the cell membrane and preventing normal budding owing to the loss of membrane integrity. Thus, obtained results (Figure 9a−e) indicated that the novel synthesized (Ag@biochar) is a promising and powerful antibacterial agent that could be used against Gram-negative and also Gram-positive bacteria with a high concentration (2×10^8 CFU/mL).

Table 1. Comparison between Ag@Biochar and Other Catalysts According to Their Photodegradation Capacity of MB

catalyst	photodegradation capacity (%)	dye concentration (mg/L)	time (min)	refs
AgNPs	82.8	60	180	69
AgNPs	92.1	25	14	70
Ag/ZnO	81.2	25	240	71
Ag/ZnO nanocomposite	94.3	10	120	72
Ag@biochar	88.4	25	75	this study
Ag@biochar	84.0	50	210	this study

The specific mechanism by which nanoparticles generate antimicrobial effects is yet unknown. However, it is suggested that when the nanoparticles come into direct contact with microbial cells, they result in cell death by disruption of the cell membrane, induction of hyperthermia, disturbance of nutrient uptake, and other physiological disorders. When a previous study was conducted by Yan *et al.*[75] to deeply investigate the antimicrobial effect of AgNPs against *P. aeruginosa*, it was concluded that the effect on membrane proteins and the oxidative stress induced by AgNPs is the main mechanism responsible for the antimicrobial activity. Various membrane proteins whose expression was allegedly regulated by AgNPs were discovered. These proteins are mainly responsible for flagellum assembly, ion binding, antibiotic resistance, and membrane stabilization. Many of these proteins, which are associated with the transport of cationic amino acids, peptides, antibiotics, and ions were considerably hindered by AgNPs. Moreover, they indicated that some metal transporters were also inhibited by AgNPs, resulting in AgNP transport into the cell through the transmembrane pores and eventually leading to bacterial disruption and death.

2.3.2. Antifungal Study. *Candida albicans* is a prevalent yeast that colonizes the skin and mucosal membranes in opportunistic fungal infections all over the world. *Candida* is an opportunistic part of the natural flora of the skin, mouth,

https://doi.org/10.1021/acsomega.1c07209
ACS Omega 2022, 7, 8046−8059

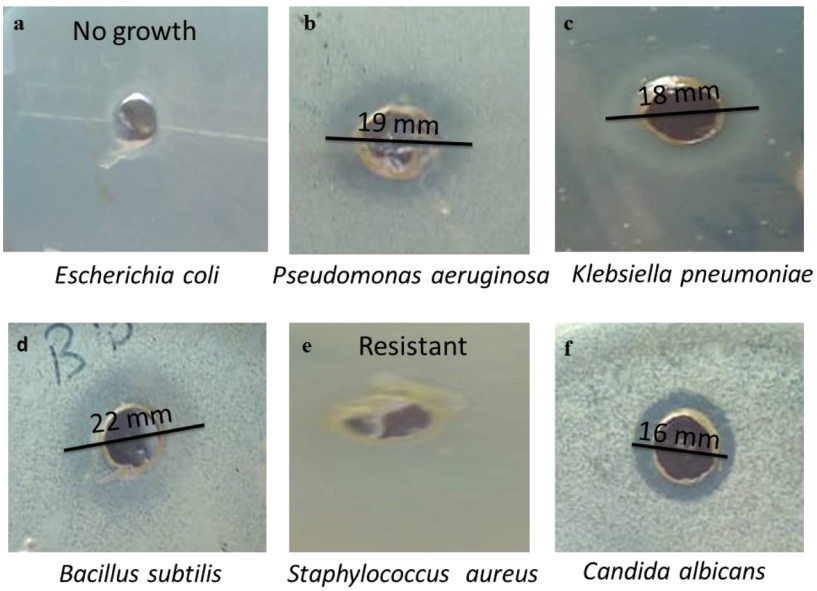

Figure 9. Antimicrobial efficiency of Ag@biochar against (a) *E. coli*, (b) *P. aeruginosa*, (c) *K. pneumoniae*, (d) *B. subtilis*, (e) *S. aureus*, and (f) *C. albicans*.

Table 2. Comparison between the Antimicrobial Efficiency of Ag@Biochar Prepared in the Current Study and AgNPs and AgNP Nanocomposites Prepared in Other Studies

sample	sample concentration (mg mL^{-1})	bacterial strain	zone of inhibition (mm)	references
chitosan−silver nanoparticles (CS−AgNPs)	1	*Escherichia coli*	10	78
methanol silver nanoparticles (SNPs)	100	*Staphylococcus aureus*	14.33	79
		Escherichia coli	10.33	
		Pseudomonas aeruginosa	13.67	
		Staphylococcus aureus	12.6	
		Staphylococcus aureus	13	
		Pseudomonas aeruginosa	16	
AgNP-embedded guar gum/gelatin nanocomposite		*Escherichia coli*	12.5	80
		Staphylococcus aureus	13	
		Pseudomonas aeruginosa	12.5	
Ag/GO nanocomposite	1	*Staphylococcus aureus*	15	81
		Escherichia coli	19	
copper−silver−titanium oxide nanocomposite (Cu−Ag−TiO_2)	0.5	*Staphylococcus aureus*	21	82
		Escherichia coli	16	
		Escherichia coli	16	
		Escherichia coli	9.3	
Ag@biochar	1	*Escherichia coli*	no growth (sensitive)	this study
		Pseudomonas aeruginosa	19	
		Klebsiella pneumoniae	18	
		Bacillus subtilis	22	
		Staphylococcus aureus	resistant	
		Candida albicans	16	

vagina, and feces. In nature, it can be found on plant leaves, water, and dirt. *C. albicans* is a pleomorphic mold that is found in human and animal bodies. It is worth noting that recent reports indicated an increased rate of *C. albicans* coinfection during the COVID-19 pandemic, with an incomplete understanding of the pathogenesis and without any causative therapy being available.[76] Therefore, the search for a new material that could be used as an antifungal agent with high efficiency is supposed to be of great importance. The green synthesized Ag@biochar in this study was tested as an antifungal agent against *C. albicans* with a high concentration (2×10^8 CFU/mL), and it did stop the growth of *Candida* with an inhibition zone of 16 mm (Figure 9f). Consequently, Ag@biochar was concluded to be an efficient and promising antifungal agent.

Regarding the antifungal mechanism, the use of Ag@biochar hinders the fungal cell wall, as well as other physiological processes. Additionally, Ag@biochar can result in DNA fragmentation and nuclear condensation during different types of cell death, as well as inhibition of the respiratory chain, induction of hyperthermia, and disturbance of nutrient uptake. Finally, all these interactions end up in fungal cell

https://doi.org/10.1021/acsomega.1c07209
ACS Omega 2022, 7, 8046−8059

Scheme 1. Schematic Representation for the Preparation of the Green Ag@Biochar

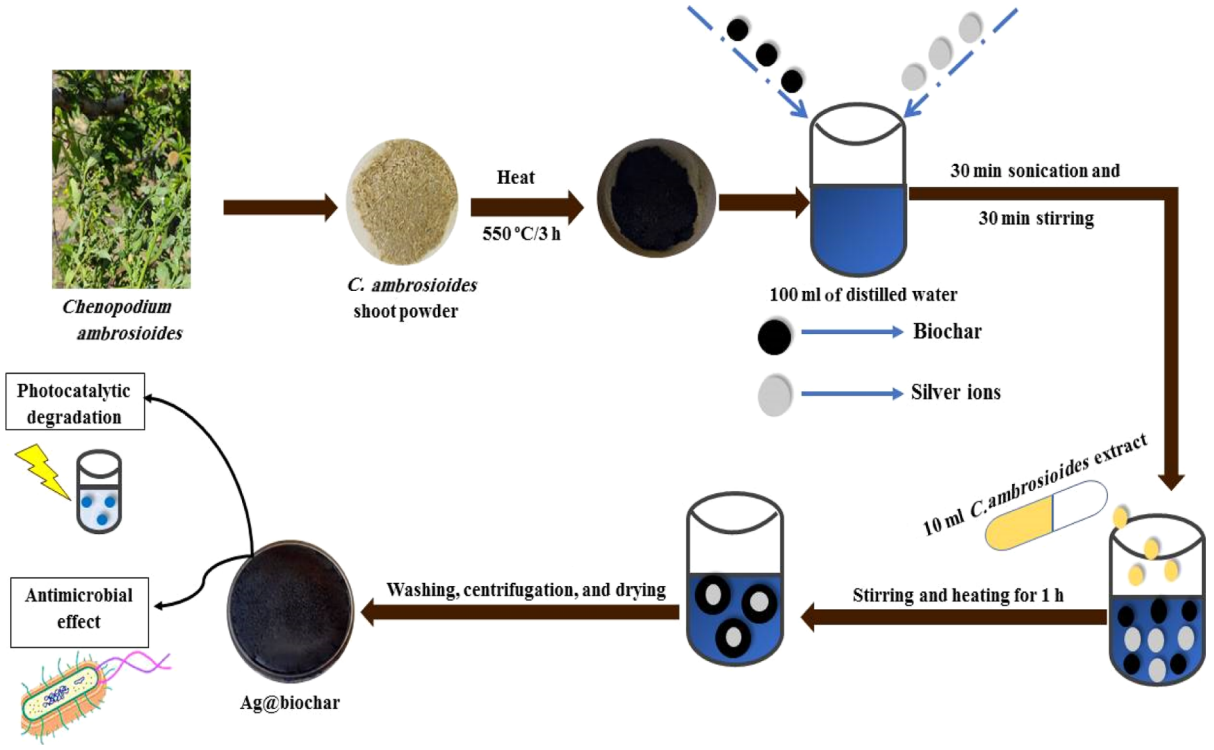

death (apoptosis), as previously mentioned by many workers.[77]

When a comparison was made among the diameters of the inhibition zone for different green synthesized samples of AgNPs and AgNP composites including the green synthesized composite (Ag@biochar) in this study in Table 2, it was concluded that the efficacy of our novel green synthesized nanocomposite was better than those of most of the nanomaterials synthesized in other studies.

Based on the current results, it was concluded that the green synthesized Ag@biochar could be considered a broad-spectrum and powerful disinfectant as it showed a good inhibitory effect against Gram-negative and Gram-positive bacteria and also fungi. Therefore, Ag@biochar could be used as a promising antimicrobial agent in wastewater treatment.

3. CONCLUSIONS

The Ag@biochar nanocomposite was synthesized for the first time using *C. ambrosioides*. Flavonoids, tannins, and alkaloids present in *C. ambrosioides* were concluded to be responsible for reducing silver ions into AgNPs on the biochar surface. AgNPs on biochar were mostly spherical with a size range of 25−35 nm. Ag@biochar acquired a surface charge of −5.87 mV, an SPR peak at 420 nm, and a surface area of 47.61 m^2/g. The synthesized Ag@biochar nanocomposite was proven to be an effective adsorbent and photocatalyst with relatively low band gap energy (1.9 eV). Also, Ag@biochar was confirmed to be photoluminescent at 425 nm. The formation of Ag^0 with a binding energy splitting difference of 6 eV was confirmed by the XPS results. The TGA results signified the higher thermal stability of Ag@biochar compared to the pristine biochar as a result of the presence of AgNPs. The removal efficiency of MB by Ag@biochar was as high as 88.4% because of its high electron transfer rate, as confirmed by the EIS analysis. Moreover, it decreased to 70.65% after six recycling times, denoting its high regeneration efficacy. In addition, the rate constant K was found to be 0.0147 min^{-1}. The complete prevention of the growth of *E. coli*, as well as the inhibition of *P. aeruginosa*, *K. pneumoniae*, *B. subtilis*, and *C. albicans* with inhibition zones of 19, 18, 22, and 16 mm, respectively, confirmed the potent antimicrobial efficiency of Ag@biochar. The obtained results indicated promising photocatalytic and disinfection properties of Ag@biochar.

4. MATERIALS AND METHODS

4.1. Materials. Silver nitrate (99.9%, $AgNO_3$) and MB dye ($C_{16}H_{18}N_3SCl$, 319.85 g/mol) were purchased from Merck, USA.

4.2. Preparation of the *C. ambrosioides* Extract. 5 g of *C. ambrosioides* was dissolved in 100 mL of deionized water (DW); then, the solution was subjected to heating and stirring at 80 °C, and finally, it was filtered and the filtrate was preserved at 4 °C for further use.

4.3. Preparation of *C. ambrosioides*-Derived Biochar. *C. ambrosioides* is a medicinal plant found in countries with a tropical, subtropical, and temperate climate and some regions of the Mediterranean and Central America. It is a naturalized and common species in moist grounds and canal banks in Egypt. The *C. ambrosioides* specimens were collected from their natural habitat on the northern coast of Egypt. The plant shoot was separated, and then it was rinsed with DW several times to remove impurities or dirt. Then, it was fragmented and allowed to dry in the open air, followed by oven-drying overnight at 60 °C. Afterward, dry stems were ground in a stainless-steel mixer to obtain a fine powder. Afterward, 10 g of the dried powder was subjected to pyrolysis in a muffle furnace at 550 °C for 3 h to obtain the biochar.

4.4. Green Synthesis of the Ag@Biochar Nanocomposite. 0.79 g of biochar powder was dispersed in 100 mL of DW; then, 0.0158 g of $AgNO_3$ was added to the biochar

https://doi.org/10.1021/acsomega.1c07209
ACS Omega 2022, 7, 8046−8059

dispersion, and it was sonicated for 30 min. Afterward, 10 mL of the *C. ambrosioides* extract was added to the solution, accompanied by stirring and heating at 80 °C for 1 h to reduce the silver ions on the surface of the biochar to form the Ag@biochar nanocomposite. The formed Ag@biochar nanocomposite was separated *via* centrifugation and washed three times with DW and ethanol. Eventually, the Ag@biochar nanocomposite was dried in an oven at 60 °C for 24 h. The procedures are meticulously provided in Scheme 1.

4.5. Characterization of the Ag@Biochar Nanocomposite. The biogenic reduction of the Ag^+ to AgNPs on the surface of biochar was confirmed *via* the UV−visible spectroscopy measurements on a double-beam spectrophotometer (T70/T80 series UV/vis spectrophotometer, PG Instruments Ltd., UK) in the scanning range of 200−800 nm. The XRD measurements of Ag@biochar nanocomposite were done on an X-ray diffractometer (X'Pert Pro, The Netherlands) operated at a voltage of 45 kV and a current of 40 mA with Cu Kα1 radiation (λ = 1.54056 Å) in the 2θ range from 20 to 80°. The crystallite size was calculated from the width of the XRD peaks using the Scherrer formula as given by

$$(D) = \frac{0.9\,\lambda}{\beta\ \cos\theta} \tag{6}$$

where D is the average crystallite size, β indicates the line broadening the value of the full width at half-maximum of a peak, λ is the wavelength of irradiated X-rays, and θ is the maximum peak position value.

The morphological structure and elemental composition analysis were investigated *via* a scanning electron microscope (JEOLJSM-IT 200, Japan) attached to an energy-dispersive X-ray (EDX) spectrometer. XPS was carried out using K-ALPHA (Thermo Fisher Scientific, USA) with monochromatic X-ray Al Kα radiation from −10 to 1350 eV with a spot size of 400 μm at a pressure of 10^{-9} mbar with full-spectrum pass energy 200 eV and narrow-spectrum 50 eV. FT-IR spectroscopy was conducted to assess the possible surface modification of biochar with AgNPs; the measurements were conducted for the ground sample with KBr using a JASCO spectrometer over the range 4000−600 cm^{-1}. The specific surface area was estimated using nitrogen adsorption/desorption isotherms (Micromeritics ASAP2020M analyzer, USA). Thermal stability was studied by TGA (Shimadzu-50, Japan). The zeta potentials of the fabricated biochar and Ag@biochar nanocomposite were examined using a zeta potential analyzer (Zetasizer Nano ZS Malvern). BET analysis was used to study the surface area, total pore volume, and pore diameter of the Ag@biochar nanocomposite using the nitrogen adsorption/desorption isotherm obtained using the multipoint BET and the BJH process methods using a BET analyzer (Quantachrome NovaWin, 1994−2013, Quantachrome Instruments v11.03). PL studies were carried out using an F-2700 FL fluorescence spectrophotometer. The EIS measurements were performed using a potentiostat/galvanostat (Gamry PCI4G750) equipped with a three-electrode cell configuration.

4.6. Photocatalytic Experiments. The photocatalytic activity of the green synthesized Ag@biochar nanocomposite against MB dye was evaluated. 5 mg of the Ag@biochar nanocomposite was added to 10 mL of three different concentrations of MB solution (10, 25, and 50 ppm). The control experiment was carried out using 5 mg of biochar with an MB solution of a concentration of 25 ppm. Both test and control solutions were mixed for 30 min under dark conditions for adsorption/desorption equilibration. Then, the solutions were stirred under a xenon lamp as a visible-light source (λ > 420 nm) and monitored. Next, 2 mL aliquots were removed and centrifuged at 17,000 rpm for 2 min to separate the solid nanocatalyst. The absorbance of the resultant supernatant of MB dye of both control and test solutions was measured at 664 nm wavelength in a quartz cuvette (path length of 1 cm) using UV−vis spectroscopy (T70/T80 series UV/vis spectrophotometer, PG Instruments Ltd., UK); scanning was done in the range of 200−800 nm. The percentage of MB dye degradation was calculated by the following formula[83]

$$\%\ \text{Degradation} = \frac{A_o}{A} \times 100 \tag{7}$$

Concerning the regeneration process, Ag@biochar was first removed from the solution *via* centrifugation at 17,000 rpm for 1 min, and then it was thoroughly washed with DW and eventually dried overnight in an oven.

4.7. Antimicrobial Test. *4.7.1. Inoculum Preparation.* After overnight incubation, the tops of each of 3−5 colonies of a pure culture of the organism to be tested [*E. coli* (ATCC 8739), *P. aeruginosa* (ATCC 9027), *K. pneumoniae* (ATCC 1388), *B. subtilis* (ATCC 6633), *S. aureus* (MRSA) (ATCC 25923), and *C. albicans* (ATCC 10231)] were touched with a loop and suspended in a sterile test tube containing 2 mL of saline. The turbidity of the suspended colonies was compared with the 0.5 McFarland turbidity standard equivalent to 2 × 10^8 CFU/mL, and the density of the organism suspension was adjusted by adding more bacteria or more sterile saline.

4.7.2. Preparation of Seeded Agar. Muller−Hinton agar was weighed, dissolved in DW, and then sterilized by autoclaving after being divided into 25 mL portions into six separate flasks. The flasks were left to cool to 50 °C, and then the tested reference strains (1%) were added onto sterile Muller−Hinton agar. The flasks were shaken and poured onto sterile Petri dishes and left to solidify. With a sterile cork borer, three wells (each 8 mm diameter) were made in each seeded agar plate.

4.7.3. Placing of the Tested Materials (Ag@Biochar). The panel of the selected material to be evaluated was placed on the inoculated plates using a sterile automatic pipette directly onto its specific well after sterilization by filtration; the plates were put in the refrigerator overnight to allow diffusion of the Ag@biochar material.

4.7.4. Incubation. The plates were incubated at 35 ± 2 °C for 24 h.

4.7.5. Reading Results. All measurements were made with the unaided eye while viewing the back of the Petri dish a few inches above a nonreflecting background and illuminated with reflected light.

4.8. Statistical Analysis. All experiments were conducted in triplicate (n = 3), while the gained data were presented as a mean value corrected by the standard deviation (±SD).

■ ASSOCIATED CONTENT

Supporting Information

The Supporting Information is available free of charge at https://pubs.acs.org/doi/10.1021/acsomega.1c07209.

XRD pattern of biochar and Ag@biochar, FTIR spectroscopy of biochar and Ag@biochar, zeta potential of biochar and Ag@biochar, time effect on the degradation of MB at the concentrations of 25 and 50

https://doi.org/10.1021/acsomega.1c07209
ACS Omega 2022, 7, 8046−8059

ppm in the presence of Ag@biochar, and possible mechanism of MB photodegradation using Ag@biochar (PDF)

AUTHOR INFORMATION

Corresponding Authors

Abdelazeem S. Eltaweil − *Department of Chemistry, Faculty of Science, Alexandria University, Alexandria 21321, Egypt;* orcid.org/0000-0001-8912-1244; Email: abdelazeemeltaweil@alexu.edu.eg

Mohamed Hosny − *Green Technology Group, Environmental Sciences Department, Faculty of Science, Alexandria University, Alexandria 21511, Egypt;* orcid.org/0000-0001-6824-5459; Email: MohamedHosny@alexu.edu.eg, mohamedhosnymetal09@gmail.com

Authors

Ahmed M. Abdelfatah − *Green Technology Group, Environmental Sciences Department, Faculty of Science, Alexandria University, Alexandria 21511, Egypt*

Manal Fawzy − *Green Technology Group, Environmental Sciences Department, Faculty of Science, Alexandria University, Alexandria 21511, Egypt; National Egyptian Biotechnology Experts Network, National Egyptian Academy for Scientific Research and Technology, Cairo 33516, Egypt;* orcid.org/0000-0002-9401-9049

Complete contact information is available at: https://pubs.acs.org/10.1021/acsomega.1c07209

Author Contributions

A.S.E. suggested the idea of this article and was responsible for conceptualization, supervision, validation, and reviewing the final manuscript. A.M.A. was responsible for conducting the laboratory experiments and writing the original draft. M.H. was responsible for the investigation, formal analysis, methodology, data curation, visualization, and writing the original draft. M.F. was responsible for conceptualization, funding acquisition, project administration, supervision, validation, and reviewing the final manuscript.

Notes

The authors declare no competing financial interest.

ACKNOWLEDGMENTS

This work was supported by SMARTWATIR, ERANETMED-3-227 project, Academy of Scientific Research and Technology.

REFERENCES

(1) Razavi-Khosroshahi, H.; Wenhao, S.; Fuji, M. Synthesis of TiO2 hollow nanoparticles with different shell thickness and effect of structure on photocatalytic activity. *Solid State Sci.* **2020**, *103*, 106179.

(2) Hidalgo-Jimenez, J.; Wang, Q.; Edalati, K.; Cubero-Sesín, J. M.; Razavi-Khosroshahi, H.; Ikoma, Y.; Gutiérrez-Fallas, D.; Dittel-Meza, F. A.; Rodríguez-Rufino, J. C.; Fuji, M.; Horita, Z. Phase transformations, vacancy formation and variations of optical and photocatalytic properties in TiO2-ZnO composites by high-pressure torsion. *Int. J. Plast.* **2020**, *124*, 170−185.

(3) Eltaweil, A. S.; Omer, A. M.; El-Aqapa, H. G.; Gaber, N. M.; Attia, N. F.; El-Subruiti, G. M.; Mohy-Eldin, M. S.; Abd El-Monaem, E. M. Chitosan based adsorbents for the removal of phosphate and nitrate: A critical review. *Carbohydr. Polym.* **2021**, *274*, 118671.

(4) Abdelfatah, A. M.; Fawzy, M.; El-Khouly, M. E.; Eltaweil, A. S. Efficient Adsorptive Removal of Tetracycline from Aqueous Solution using Phytosynthesized Nano-zero Valent Iron. *J. Saudi Chem. Soc.* **2021**, *25*, 101365.

(5) Eltaweil, A. S.; Mamdouh, I. M.; Abd El-Monaem, E. M.; El-Subruiti, G. M. Highly efficient removal for methylene blue and Cu2+ onto UiO-66 metal−organic framework/carboxylated graphene oxide-incorporated sodium alginate beads. *ACS Omega* **2021**, *6*, 23528−23541.

(6) Omer, A. M.; Dey, R.; Eltaweil, A. S.; Abd El-Monaem, E. M.; Ziora, Z. M. Insights into recent advances of chitosan-based adsorbents for sustainable removal of heavy metals and anions. *Arabian J. Chem.* **2022**, *15*, 103543.

(7) Li, Y.; Wang, H.; Xie, J.; Hou, J.; Song, X.; Dionysiou, D. D. Bi2WO6-TiO2/starch composite films with Ag nanoparticle irradiated by γ-ray used for the visible light photocatalytic degradation of ethylene. *Chem. Eng. Sci.* **2021**, *421*, 129986.

(8) Hosny, M.; Fawzy, M.; Abdelfatah, A. M.; Fawzy, E. E.; Eltaweil, A. S. Comparative study on the potentialities of two halophytic species in the green synthesis of gold nanoparticles and their anticancer, antioxidant and catalytic efficiencies. *Adv. Powder Technol.* **2021**, *32*, 3220−3233.

(9) Hosny, M.; Fawzy, M.; El-Badry, Y. A.; Hussein, E. E.; Eltaweil, A. S. Plant-assisted synthesis of gold nanoparticles for photocatalytic, anticancer, and antioxidant applications. *J. Saudi Chem. Soc.* **2022**, *26*, 101419.

(10) Abdelfatah, A. M.; Fawzy, M.; Eltaweil, A. S.; El-Khouly, M. E. Green Synthesis of Nano-Zero-Valent Iron Using Ricinus Communis Seeds Extract: Characterization and Application in the Treatment of Methylene Blue-Polluted Water. *ACS Omega* **2021**, *6*, 25397−25411.

(11) Zinatloo-Ajabshir, S.; Morassaei, M. S.; Salavati-Niasari, M. Eco-friendly synthesis of Nd2Sn2O7−based nanostructure materials using grape juice as green fuel as photocatalyst for the degradation of erythrosine. *Composites, Part B* **2019**, *167*, 643−653.

(12) El-Borady, O. M.; Fawzy, M.; Hosny, M. Antioxidant, anticancer and enhanced photocatalytic potentials of gold nanoparticles biosynthesized by common reed leaf extract. *Appl. Nanosci.* **2021**, 1−12.

(13) Hosny, M.; Eltaweil, A. S.; Mostafa, M.; El-Badry, Y. A.; Hussein, E. E.; Omer, A. M.; Fawzy, M. Facile Synthesis of Gold Nanoparticles for Anticancer, Antioxidant Applications, and Photocatalytic Degradation of Toxic Organic Pollutants. *ACS Omega* **2022**, *7*, 3121−3133.

(14) Pan, X.; Gu, Z.; Chen, W.; Li, Q. Preparation of biochar and biochar composites and their application in a Fenton-like process for wastewater decontamination: A review. *Sci. Total Environ.* **2021**, *754*, 142104.

(15) Wang, B.; Jiang, Y.-s.; Li, F.-y.; Yang, D.-y. Preparation of biochar by simultaneous carbonization, magnetization and activation for norfloxacin removal in water. *Bioresour. Technol.* **2017**, *233*, 159−165.

(16) Wang, J.; Wang, S. Preparation, modification and environmental application of biochar: a review. *J. Cleaner Prod.* **2019**, *227*, 1002−1022.

(17) Gong, H.; Tan, Z.; Zhang, L.; Huang, Q. Preparation of biochar with high absorbability and its nutrient adsorption−desorption behaviour. *Sci. Total Environ.* **2019**, *694*, 133728.

(18) Zand, A. D.; Tabrizi, A. M.; Heir, A. V. Incorporation of biochar and nanomaterials to assist remediation of heavy metals in soil using plant species. *Environ. Technol. Innovation* **2020**, *20*, 101134.

(19) Premarathna, K. S. D.; Rajapaksha, A. U.; Adassoriya, N.; Sarkar, B.; Sirimuthu, N. M. S.; Cooray, A.; Ok, Y. S.; Vithanage, M. Clay-biochar composites for sorptive removal of tetracycline antibiotic in aqueous media. *J. Environ. Manage.* **2019**, *238*, 315−322.

(20) Cho, D.-W.; Yoon, K.; Ahn, Y.; Sun, Y.; Tsang, D. C. W.; Hou, D.; Ok, Y. S.; Song, H. Fabrication and environmental applications of multifunctional mixed metal-biochar composites (MMBC) from red mud and lignin wastes. *J. Hazard. Mater.* **2019**, *374*, 412−419.

(21) Yu, I. K. M.; Xiong, X.; Tsang, D. C.; Wang, L.; Hunt, A. J.; Song, H.; Shang, J.; Ok, Y. S.; Poon, C. S. Aluminium-biochar

composites as sustainable heterogeneous catalysts for glucose isomerisation in a biorefinery. *Green Chem.* **2019**, *21*, 1267−1281.
(22) Sun, Y.; Yu, I. K. M.; Tsang, D. C. W.; Cao, X.; Lin, D.; Wang, L.; Graham, N. J. D.; Alessi, D. S.; Komárek, M.; Ok, Y. S.; Feng, Y.; Li, X.-D. Multifunctional iron-biochar composites for the removal of potentially toxic elements, inherent cations, and hetero-chloride from hydraulic fracturing wastewater. *Environ. Int.* **2019**, *124*, 521−532.
(23) Monsef, R.; Ghiyasiyan-Arani, M.; Amiri, O.; Salavati-Niasari, M. Sonochemical synthesis, characterization and application of PrVO4 nanostructures as an effective photocatalyst for discoloration of organic dye contaminants in wastewater. *Ultrason. Sonochem.* **2020**, *61*, 104822.
(24) Monsef, R.; Ghiyasiyan-Arani, M.; Salavati-Niasari, M. Utilizing of neodymium vanadate nanoparticles as an efficient catalyst to boost the photocatalytic water purification. *J. Environ. Manage.* **2019**, *230*, 266−281.
(25) Mortazavi-Derazkola, S.; Zinatloo-Ajabshir, S.; Salavati-Niasari, M. Novel simple solvent-less preparation, characterization and degradation of the cationic dye over holmium oxide ceramic nanostructures. *Ceram. Int.* **2015**, *41*, 9593−9601.
(26) Monsef, R.; Ghiyasiyan-Arani, M.; Salavati-Niasari, M. Design of Magnetically Recyclable Ternary Fe2O3/EuVO4/g-C3N4 Nanocomposites for Photocatalytic and Electrochemical Hydrogen Storage. *ACS Appl. Energy Mater.* **2021**, *4*, 680−695.
(27) Zhu, K.; Bin, Q.; Shen, Y.; Huang, J.; He, D.; Chen, W. In-situ formed N-doped bamboo-like carbon nanotubes encapsulated with Fe nanoparticles supported by biochar as highly efficient catalyst for activation of persulfate (PS) toward degradation of organic pollutants. *Chem. Eng. J.* **2020**, *402*, 126090.
(28) Niu, Z.; Feng, W.; Huang, H.; Wang, B.; Chen, L.; Miao, Y.; Su, S. Green synthesis of a novel Mn−Zn ferrite/biochar composite from waste batteries and pine sawdust for Pb2+ removal. *Chemosphere* **2020**, *252*, 126529.
(29) Hosny, M.; Fawzy, M. Instantaneous phytosynthesis of gold nanoparticles via Persicaria salicifolia leaf extract, and their medical applications. *Adv. Powder Technol.* **2021**, *32*, 2891−2904.
(30) Hosny, M.; Fawzy, M.; El-Fakharany, E. M.; Omer, A. M.; El-Monaem, E. M. A.; Khalifa, R. E.; Eltaweil, A. S. Biogenic synthesis, characterization, antimicrobial, antioxidant, antidiabetic, and catalytic applications of platinum nanoparticles synthesized from Polygonum salicifolium leaves. *J. Environ. Chem. Eng.* **2022**, *10*, 106806.
(31) El-Maghrabi, N.; El-Borady, O. M.; Hosny, M.; Fawzy, M. Catalytic and Medical Potential of a Phyto-Functionalized Reduced Graphene Oxide−Gold Nanocomposite Using Willow-Leaved Knotgrass. *ACS Omega* **2021**, *6*, 34954−34966.
(32) Ghanbari, D.; Salavati-Niasari, M.; Sabet, M. Preparation of flower-like magnesium hydroxide nanostructure and its influence on the thermal stability of poly vinyl acetate and poly vinyl alcohol. *Composites, Part B* **2013**, *45*, 550−555.
(33) Salavati-Niasari, M.; Sobhani, A.; Davar, F. Synthesis of star-shaped PbS nanocrystals using single-source precursor. *J. Alloys Compd.* **2010**, *507*, 77−83.
(34) Salavati-Niasari, M.; Davar, F.; Fereshteh, Z. Synthesis of nickel and nickel oxide nanoparticles via heat-treatment of simple octanoate precursor. *J. Alloys Compd.* **2010**, *494*, 410−414.
(35) Salavati-Niasari, M.; Ghanbari, D.; Davar, F. Synthesis of different morphologies of bismuth sulfide nanostructures via hydrothermal process in the presence of thioglycolic acid. *J. Alloys Compd.* **2009**, *488*, 442−447.
(36) Salavati-Niasari, M.; Davar, F.; Mazaheri, M. Synthesis of Mn3O4 nanoparticles by thermal decomposition of a [bis (salicylidiminato) manganese (II)] complex. *Polyhedron* **2008**, *27*, 3467−3471.
(37) Salavati-Niasari, M. Nanoscale microreactor-encapsulation 14-membered nickel(II) hexamethyl tetraaza: synthesis, characterization and catalytic activity. *J. Mol. Catal. A: Chem.* **2005**, *229*, 159−164.
(38) LewisOscar, F.; Nithya, C.; Vismaya, S.; Arunkumar, M.; Pugazhendhi, A.; Nguyen-Tri, P.; Alharbi, S. A.; Alharbi, N. S.; Thajuddin, N. In vitro analysis of green fabricated silver nanoparticles (AgNPs) against Pseudomonas aeruginosa PA14 biofilm formation, their application on urinary catheter. *Prog. Org. Coat.* **2021**, *151*, 106058.
(39) Fazal, T.; Razzaq, A.; Javed, F.; Hafeez, A.; Rashid, N.; Amjad, U. S.; Ur Rehman, M. S.; Faisal, A.; Rehman, F. Integrating adsorption and photocatalysis: A cost effective strategy for textile wastewater treatment using hybrid biochar-TiO2 composite. *J. Hazard. Mater.* **2020**, *390*, 121623.
(40) Wang, T.; Liu, S.; Mao, W.; Bai, Y.; Chiang, K.; Shah, K.; Paz-Ferreiro, J. Novel Bi2WO6 loaded N-biochar composites with enhanced photocatalytic degradation of rhodamine B and Cr (VI). *J. Hazard. Mater.* **2020**, *389*, 121827.
(41) Ansari, F.; Sobhani, A.; Salavati-Niasari, M. Green synthesis of magnetic chitosan nanocomposites by a new sol−gel auto-combustion method. *J. Magn. Magn. Mater.* **2016**, *410*, 27−33.
(42) Omer, A. M.; Abd El-Monaem, E. M.; El-Subruiti, G. M.; Abd El-Latif, M. M.; Eltaweil, A. S.; Mona, M.; Eltaweil, A. S. Fabrication of easy separable and reusable MIL-125 (Ti)/MIL-53 (Fe) binary MOF/CNT/Alginate composite microbeads for tetracycline removal from water bodies. *Sci. Rep.* **2021**, *11*, 23818.
(43) Dai, W.; Xu, M.; Zhao, Z.; Zheng, J.; Huang, F.; Wang, H.; Liu, C.; Xiao, R. Characteristics and quantification of mechanisms of Cd2+ adsorption by biochars derived from three different plant-based biomass. *Arabian J. Chem.* **2021**, *14*, 103119.
(44) Rajkumar, R.; Ezhumalai, G.; Gnanadesigan, M. A green approach for the synthesis of silver nanoparticles by Chlorella vulgaris and its application in photocatalytic dye degradation activity. *Environ. Technol. Innovation* **2021**, *21*, 101282.
(45) Zinatloo-Ajabshir, S.; Morassaei, M. S.; Amiri, O.; Salavati-Niasari, M. Green synthesis of dysprosium stannate nanoparticles using Ficus carica extract as photocatalyst for the degradation of organic pollutants under visible irradiation. *Ceram. Int.* **2020**, *46*, 6095−6107.
(46) Hashim, N.; Paramasivam, M.; Tan, J. S.; Kernain, D.; Hussin, M. H.; Brosse, N.; Gambier, F.; Raja, P. B. Green mode synthesis of silver nanoparticles using Vitis vinifera's tannin and screening its antimicrobial activity/apoptotic potential versus cancer cells. *Mater. Today Commun.* **2020**, *25*, 101511.
(47) Dai, Z.; Meng, J.; Muhammad, N.; Liu, X.; Wang, H.; He, Y.; Brookes, P. C.; Xu, J. The potential feasibility for soil improvement, based on the properties of biochars pyrolyzed from different feedstocks. *J. Soils Sediments* **2013**, *13*, 989−1000.
(48) Adeniyi, A. G.; Ighalo, J. O.; Onifade, D. V. Biochar from the thermochemical conversion of orange (Citrus sinensis) peel and Albedo: product quality and potential applications. *Chem. Afr.* **2020**, *3*, 439−448.
(49) Ma, Z.; Liu, J.; Liu, Y.; Zheng, X.; Tang, K. Green synthesis of silver nanoparticles using soluble soybean polysaccharide and their application in antibacterial coatings. *Int. J. Biol. Macromol.* **2021**, *166*, 567−577.
(50) Fleutot, S.; Martinez, H.; Dupin, J. C.; Baraille, I.; Forano, C.; Renaudin, G.; Gonbeau, D. Experimental (X-Ray Photoelectron Spectroscopy) and theoretical studies of benzene based organics intercalated into layered double hydroxide. *Solid State Sci.* **2011**, *13*, 1676−1686.
(51) Zotti, G.; Zecchin, S.; Schiavon, G.; Louwet, F.; Groenendaal, L.; Crispin, X.; Osikowicz, W.; Salaneck, W.; Fahlman, M. Electrochemical and XPS studies toward the role of monomeric and polymeric sulfonate counterions in the synthesis, composition, and properties of poly (3, 4-ethylenedioxythiophene). *Macromolecules* **2003**, *36*, 3337−3344.
(52) Xi, Y.; Sun, Z.; Hreid, T.; Ayoko, G. A.; Frost, R. L. Bisphenol A degradation enhanced by air bubbles via advanced oxidation using in situ generated ferrous ions from nano zero-valent iron/palygorskite composite materials. *Chem. Eng. J.* **2014**, *247*, 66−74.
(53) Liu, Y.; Yang, S.; Yin, S.-N.; Feng, L.; Zang, Y.; Xue, H. In situ construction of fibrous AgNPs/g-C3N4 aerogel toward light-driven COx-free methanol dehydrogenation at room temperature. *Chem. Eng. J.* **2018**, *334*, 2401−2407.

https://doi.org/10.1021/acsomega.1c07209
ACS Omega 2022, 7, 8046−8059

(54) Ghodake, G.; Kim, M.; Sung, J.-S.; Shinde, S.; Yang, J.; Hwang, K.; Kim, D.-Y. Extracellular synthesis and characterization of silver nanoparticles—Antibacterial activity against multidrug-resistant bacterial strains. *Nanomaterials* **2020**, *10*, 360.
(55) Hosny, M.; Fawzy, M.; El-Borady, O. M.; Mahmoud, A. E. D. Comparative study between Phragmites australis root and rhizome extracts for mediating gold nanoparticles synthesis and their medical and environmental applications. *Adv. Powder Technol.* **2021**, *32*, 2268−2279.
(56) Hamouda, R. A.; Abd El-Mongy, M.; Eid, K. F. Comparative study between two red algae for biosynthesis silver nanoparticles capping by SDS: Insights of characterization and antibacterial activity. *Microb. Pathog.* **2019**, *129*, 224−232.
(57) Eltaweil, A. S.; Ali Mohamed, H.; Abd El-Monaem, E. M.; El-Subruiti, G. M. Mesoporous magnetic biochar composite for enhanced adsorption of malachite green dye: Characterization, adsorption kinetics, thermodynamics and isotherms. *Adv. Powder Technol.* **2020**, *31*, 1253−1263.
(58) Mansaray, K.; Ghaly, A. Thermal degradation of rice husks in nitrogen atmosphere. *Bioresour. Technol.* **1998**, *65*, 13−20.
(59) Vinay, S.; Nagarju, G.; Chandrappa, C.; Chandrasekhar, N. Enhanced photocatalysis, photoluminescence, and anti-bacterial activities of nanosize Ag: green synthesized via Rauvolfia tetraphylla (devil pepper). *SN Appl. Sci.* **2019**, *1*, 477.
(60) Vigneshwaran, N.; Ashtaputre, N. M.; Varadarajan, P. V.; Nachane, R. P.; Paralikar, K. M.; Balasubramanya, R. H. Biological synthesis of silver nanoparticles using the fungus Aspergillus flavus. *Mater. Lett.* **2007**, *61*, 1413−1418.
(61) Verma, A.; Mehata, M. S. Controllable synthesis of silver nanoparticles using Neem leaves and their antimicrobial activity. *J. Radiat. Res. Appl. Sci.* **2016**, *9*, 109−115.
(62) Wang, Y.; Bai, X.; Pan, C.; He, J.; Zhu, Y. Enhancement of photocatalytic activity of Bi 2 WO 6 hybridized with graphite-like C 3 N 4. *J. Mater. Chem.* **2012**, *22*, 11568−11573.
(63) Zhang, C.; Chao, L.; Zhang, Z.; Zhang, L.; Li, Q.; Fan, H.; Zhang, S.; Liu, Q.; Qiao, Y.; Tian, Y.; Wang, Y.; Hu, X. Pyrolysis of cellulose: Evolution of functionalities and structure of bio-char versus temperature. *Renewable Sustainable Energy Rev.* **2021**, *135*, 110416.
(64) Ji, X.; Kan, G.; Jiang, X.; Sun, B.; Zhu, M.; Sun, Y. A monodisperse anionic silver nanoparticles colloid: Its selective adsorption and excellent plasmon-induced photodegradation of Methylene Blue. *J. Colloid Interface Sci.* **2018**, *523*, 98−109.
(65) Yang, S.-F.; Niu, C.-G.; Huang, D.-W.; Zhang, H.; Liang, C.; Zeng, G.-M. SrTiO 3 nanocubes decorated with Ag/AgCl nanoparticles as photocatalysts with enhanced visible-light photocatalytic activity towards the degradation of dyes, phenol and bisphenol A. *Environ. Sci.: Nano* **2017**, *4*, 585−595.
(66) Wacławek, S. Do we still need a laboratory to study advanced oxidation processes? A review of the modelling of radical reactions used for water treatment. *Ecol. Chem. Eng. S* **2021**, *28*, 11−28.
(67) Pirgholi-Givi, G.; Farjami-Shayesteh, S.; Azizian-Kalandaragh, Y. The influence of irradiation intensity and stirring rate on the photocatalytic activity of titanium dioxide nanostructures prepared by the microwave-assisted method for photodegradation of MB from water. *Phys. B* **2020**, *578*, 411886.
(68) Riaz, A.; Ashraf, A.; Taimoor, H.; Javed, S.; Akram, M. A.; Islam, M.; Mujahid, M.; Ahmad, I.; Saeed, K. Photocatalytic and photostability behavior of Ag-and/or Al-Doped ZnO films in methylene blue and rhodamine B under UV-C irradiation. *Coatings* **2019**, *9*, 202.
(69) Singh, J.; Dhaliwal, A. S. Plasmon-induced photocatalytic degradation of methylene blue dye using biosynthesized silver nanoparticles as photocatalyst. *Environ. Technol.* **2020**, *41*, 1520−1534.
(70) Fairuzi, A. A.; Bonnia, N. N.; Akhir, R. M.; Abrani, M. A.; Akil, H. M. Degradation of methylene blue using silver nanoparticles synthesized fromimperata cylindricaaqueous extract. *IOP Conf. Ser. Earth Environ. Sci.* **2018**, *105*, 012018.
(71) Abdel Messih, M. F.; Ahmed, M. A.; Soltan, A.; Anis, S. S. Synthesis and characterization of novel Ag/ZnO nanoparticles for photocatalytic degradation of methylene blue under UV and solar irradiation. *J. Phys. Chem. Solids* **2019**, *135*, 109086.
(72) Panchal, P.; Paul, D. R.; Sharma, A.; Choudhary, P.; Meena, P.; Nehra, S. P. Biogenic mediated Ag/ZnO nanocomposites for photocatalytic and antibacterial activities towards disinfection of water. *J. Colloid Interface Sci.* **2020**, *563*, 370−380.
(73) Attia, N. F.; Eid, A. M.; Soliman, M. A.; Nagy, M. Exfoliation and decoration of graphene sheets with silver nanoparticles and their antibacterial properties. *J. Polym. Environ.* **2018**, *26*, 1072−1077.
(74) Attia, N. F.; Park, J.; Oh, H. Facile tool for green synthesis of graphene sheets and their smart free-standing UV protective film. *Appl. Surf. Sci.* **2018**, *458*, 425−430.
(75) Yan, X.; He, B.; Liu, L.; Qu, G.; Shi, J.; Hu, L.; Jiang, G. Antibacterial mechanism of silver nanoparticles in Pseudomonas aeruginosa: proteomics approach. *Metallomics* **2018**, *10*, 557−564.
(76) Moser, D.; Biere, K.; Han, B.; Hoerl, M.; Schelling, G.; Choukér, A.; Woehrle, T. COVID-19 Impairs Immune Response to Candida albicans. *Front. Immunol.* **2021**, *12*, 640644.
(77) Varghese, R.; Almalki, M. A.; Ilavenil, S.; Rebecca, J.; Choi, K. C. Silver nanopaticles synthesized using the seed extract of Trigonella foenum-graecum L. and their antimicrobial mechanism and anticancer properties. *Saudi J. Biol. Sci.* **2019**, *26*, 148−154.
(78) Tharani, S.; Bharathi, D.; Ranjithkumar, R. Extracellular green synthesis of chitosan-silver nanoparticles using Lactobacillus reuteri for antibacterial applications. *Biocatal. Agric. Biotechnol.* **2020**, *30*, 101838.
(79) Yousaf, H.; Mehmood, A.; Ahmad, K. S.; Raffi, M. Green synthesis of silver nanoparticles and their applications as an alternative antibacterial and antioxidant agents. *Mater. Sci. Eng., C* **2020**, *112*, 110901.
(80) Khan, N.; Kumar, D.; Kumar, P. Silver nanoparticles embedded guar gum/gelatin nanocomposite: Green synthesis, characterization and antibacterial activity. *Colloid Interface Sci. Commun.* **2020**, *35*, 100242.
(81) Jeronsia, J. E.; Ragu, R.; Sowmya, R.; Mary, A. J.; Das, S. J. Comparative investigation on Camellia Sinensis mediated green synthesis of Ag and Ag/GO nanocomposites for its anticancer and antibacterial efficacy. *Surf. Interfaces* **2020**, *21*, 100787.
(82) Ghosh, M.; Mandal, S.; Roy, A.; Paladhi, A.; Mondal, P.; Hira, S. K.; Mukhopadhyay, S. K.; Pradhan, S. K. Synthesis and characterization of a novel drug conjugated copper-silver-titanium oxide nanocomposite with enhanced antibacterial activity. *J. Drug Delivery Sci. Technol.* **2021**, *62*, 102384.
(83) Eltaweil, A. S.; Fawzy, M.; Hosny, M.; Abd El-Monaem, E. M.; Tamer, T. M.; Omer, A. M. Green synthesis of platinum nanoparticles using Atriplex halimus leaves for potential antimicrobial, antioxidant, and catalytic applications. *Arabian J. Chem.* **2022**, *15*, 103517.

https://doi.org/10.1021/acsomega.1c07209
ACS Omega 2022, 7, 8046−8059